A radar reflectivity data assimilation method based on background-dependent hydrometeor retrieval: An observing system simulation experiment

Haiqin Chen[a], Yaodeng Chen[a,*], Jidong Gao[b], Tao Sun[a], Jacob T. Carlin[c]

[a] Key Laboratory of Meteorological Disaster of Ministry of Education (KLME) / Joint International Research Laboratory of Climate and Environment Change (ILCEC) / Collaborative Innovation Center on Forecast and Evaluation of Meteorological Disasters, Nanjing University of Information Science & Technology, Nanjing 210044, China

[b] NOAA/National Severe Storms Laboratory, Norman, Oklahoma

[c] Cooperative Institute for Mesoscale Meteorological Studies, University of Oklahoma, and NOAA/OAR National Severe Storms Laboratory, Norman, Oklahoma

June 2019

* Corresponding author:

Dr. Yaodeng Chen, keyu@nuist.edu.cn

Address:

Nanjing University of Information Science & Technology, Nanjing, China, 210044.

Abstract

Radar reflectivity contains information about hydrometeors and plays an important role in the initialization of convective-scale numerical weather prediction (NWP). In this study, a new background-dependent hydrometeor retrieval method is proposed and retrieved hydrometeors are assimilated into the Weather Research and Forecasting model (WRF), with the aim of improving short-term severe weather forecasts. Compared to traditional approaches that are mostly empirical and static, the retrieval parameters for hydrometeor identification and reflectivity partitioning in the new scheme are extracted in real-time based on the background hydrometeor fields and observed radar reflectivity. It was found that the contributions of hydrometeors to reflectivity change a lot in different reflectivity ranges and heights, indicating that adaptive parameters are necessary for reflectivity partitioning and hydrometeor retrieval. The accuracy of the background-dependent hydrometeor retrieval method and its impact on the subsequent assimilation and forecast was examined through observing system simulation experiments (OSSEs). Results show that by incorporating the background information, the retrieval accuracy was greatly improved, especially in mixed-hydrometeor regions. The assimilation of retrieved hydrometeors helped improve both the hydrometeor analyses and forecasts. With an hourly update cycling configuration, more accurate hydrometeor information was properly transferred to other model variables, such as temperature and humidity fields through the model integration, leading to an improvement of the short-term (0-3 h) precipitation forecasts.

Keywords:

Data assimilation, Radar reflectivity, Hydrometeor retrieval, Convective-scale numerical weather prediction

1. Introduction

Convective-scale data assimilation (DA) and forecasts are a primary focus and challenge of research and operations due to the important role of severe weather analyses and forecasts for saving life and property. Compared to conventional observations, which are insufficient for resolving convective-scale weather, radar data are particularly well-suited as they can capture the occurrence, development and dissipation of convection structures with abundant three-dimensional information at a high temporal and spatial resolution. It has thus been recognized that the optimal use of radar observations critically determines the quality of short-term convective weather prediction (Lilly et al., 1990; Sun et al., 2014).

Radar radial velocity seems to be natural fit for variational (Sun and Crook, 1997; Gao et al., 2004) or Ensemble Kalman Filter (EnKF, Tong and Xue, 2005) assimilation systems as it is relatively easily transformed into model state variables, while reflectivity (*Z*) assimilation at the convective scale remains a challenge. To assimilate radar reflectivity, the model state variables should be transformed to the observed reflectivity properly so that a direct comparison between observations and background fields can be drawn. One paradigm is using observation operators which convert the model variables to the observed ones. Many efforts have been devoted to the construction of observational operators for reflectivity (Xiao et al., 2007; Jung et al., 2008; Gao and Stensrud, 2012; Wang et al., 2019) and their application in both EnKF and variational methods has shown promising results. In EnKF methods, highly nonlinear operators can be implemented (Putnam et al., 2019). However, in variational assimilation systems, the incremental approach is usually adopted, which requires linearized observation forward operators. Sometimes the linearization of nonlinear observational operators under the variational DA framework will result in significant errors (Wang et al., 2013). The other paradigm is to retrieve the model variables directly from the radar reflectivity and then assimilate these variables. A variety of studies focusing on the assimilation of retrieved humidity found improved analyses and forecasts in convective regions (Lopez and Bauer, 2007; Caumont et al., 2010; Wang et al., 2013, Lai et al., 2019). Radar reflectivity also contains information about hydrometeors, such as rainwater, snow and graupel, which play a vital role in the microphysical processes for NWP (Bauer et al., 2011; Kerr et al., 2015). In order to make better use of the hydrometeor information contained in the radar reflectivity, many studies have utilized the hydrometeors retrieved from reflectivity for analysis or providing initial conditions for convective-scale NWP models (Sun and Crook, 1998; Wu et al., 2000; Hu et al., 2006; Yokota et al., 2016; Carlin et al., 2016; Wang et al., 2018).

Some earlier studies only considered warm rain processes and retrieved the rainwater mixing ratio from reflectivity observations (Sun and Crook, 1998; Wang et al., 2013). However, the inclusion of both liquid and ice-phased particles in the analysis is important for convective systems, especially deep moist convective storms (Gao and Stensrud, 2012). Generally, the dominant hydrometeor type can be determined based on the reflectivity and the background temperature thresholds. For example, an empirical reflectivity threshold of 32 dBZ is usually used to classify the graupel-dominant (>=32 dBZ) or snow-dominant (<32 dBZ) regions above the freezing level (Lerach et al., 2010; Pan et al., 2016). Besides reflectivity and temperature thresholds, additional observations have been used to improve the identification of hydrometeors types. Wang et al. (2018) discerned the graupel-dominant regions by incorporating simulated flash extent densities (FED) data from the Feng-Yun-4 geostationary satellite. Dual-polarization radar observations have also been used to improve the accuracy of hydrometeor classification (Zhang et al., 2019; Matsui et al., 2019). Once the dominant species has been defined, the total reflectivity can then be partitioned proportionally for multiple hydrometeor variables. The mixing ratio (q) of each hydrometeor is then obtained according to a Z-q formula (Carlin et al., 2016). For example, in the hydrometeor retrieval method adopted in the indirect assimilation of reflectivity in the current WRFDA, the proportion of snow and graupel is a fixed value and the contribution of rainwater increases linearly from 0 to 1 between -5 ℃ to 5 ℃; trapezoidal weighting functions corresponding to the ambient temperature profile were also utilized for graupel and snow aggregates in some studies (Zrnić et al., 2001; Wang et al., 2018).

The parameter settings of *Z* and *T* thresholds to classify hydrometer species in the above hydrometeor retrieval method are empirical, and when multiple species coexist, the partitioning process is also based on empirical rules. In actuality, the distribution characteristics of hydrometers varies in different regions and weather situations, so the fixed thresholds and proportion are likely not applicable to all cases. These empirical rules result in great uncertainty of the retrieved hydrometeors, which may limit their value for storm-scale NWP (Gao et al., 2009). Therefore, how to determine the hydrometeor types and the proportion of each species during the reflectivity retrieval under different weather conditions remains a problem worth exploring.

To overcome these problems, we propose a new method that aims to improve the hydrometeor retrieval from radar reflectivity by making the process adaptive. In the new scheme, the hydrometeors are retrieved according to their real-time contributions to reflectivity at different reflectivity intervals and heights from the model background fields so that the retrieval parameters (i.e., composition and proportions of the hydrometers) are adaptively adjusted with the evolution of weather conditions. Then, the retrieved hydrometeors are assimilated into the WRF model with the goal of improving the convective-scale analyses and forecasts. For the data assimilation method, the 3DVar method developed for the WRF model is chosen instead of more advanced methods like 4DVar, EnKF, or hybrid methods because fast and efficient analysis is essential for convective-scale weather where analyses and forecasts need to be delivered quickly to the public. Finally, the accuracy of the hydrometeor retrieval method and its impact on the subsequent assimilation and forecast is examined through observing system simulation experiments (OSSEs).

This paper is organized as follows. First, the 3DVar method, reflectivity formula, and the newly proposed "background-dependent" hydrometeor retrieval method are presented in section 2. Then, model configurations and experimental design are given in section 3. The accuracy of the background-dependent hydrometeor retrieval method and its performance on analysis and subsequent short-term forecasting are discussed in section 4 and 5. Finally, conclusions and discussions are given in section 6.

2. Methods

2.1 3DVar assimilation of radar observations

In this study, the three-dimensional variational (3DVar, Barker et al., 2012) method is employed to assimilate radial velocities and hydrometeors retrieved from radar reflectivity. The optimal analysis of 3DVar is obtained by iteratively minimizing the following cost function:

$$J(\mathbf{x}) = J_b + J_o = \frac{1}{2}\left(\mathbf{x}-\mathbf{x}^b\right)^{\mathrm{T}}\mathbf{B}^{-1}\left(\mathbf{x}-\mathbf{x}^b\right) + \frac{1}{2}\left(H(\mathbf{x})-\mathbf{y}^o\right)^{\mathrm{T}}\mathbf{R}^{-1}\left(H(\mathbf{x})-\mathbf{y}^o\right), \quad (1)$$

where J_b and J_o are the background and observational terms, respectively. The vector $\mathbf{x}$ is the analysis model state variables, $\mathbf{x}^\mathrm{b}$ is the background state, $\mathbf{y}^\mathrm{o}$ is the observation field, H is the observation operator, and $\mathbf{B}$ and $\mathbf{R}$ are the background error covariance and the observation error covariance matrices, respectively.

Observation $\mathbf{y}^\mathrm{o}$ includes the radial velocity and retrieved hydrometeors. For the indirect assimilation, reflectivity is converted to hydrometeor mixing ratios of rain, snow and graupel. These hydrometeors are then assimilated through the 3DVar system, and the analysis field is obtained through the minimization of the cost function, with the accuracy of the data assimilation dependent on the joint action of the background and observation error covariances.

2.2 Hydrometeor retrieval method for radar reflectivity

The equivalent reflectivity factor (Z_e) is obtained by summing the backscattering from particles in the atmosphere (Tong and Xue, 2005):

$$Z_e = Z(q_r) + Z(q_s) + Z(q_g), \quad (2)$$

where $Z(q_r)$, $Z(q_s)$ and $Z(q_g)$ are the reflectivity factors (here in linear units of $\mathrm{mm}^6\ \mathrm{m}^{-3}$) of rain, snow and graupel, respectively. Calculation of the equivalent reflectivity factors contributed by each species can be simplified to a Z-q relation, which is expressed most generally as

$$Z\left(q_x\right)=a_x\left(\rho q_x\right)^{1.75}, \tag{3}$$

where ρ is the air density, q_x is the mixing ratio of hydrometeor species x (e.g., "r" for rain, "s" for snow or "g" for graupel), a_x is the coefficient determined by the dielectric factor, density and intercept parameter of hydrometeor x, and Rayleigh scattering is assumed to occur. As in previous studies, a_x is frequently treated as a constant, where a_r (for rain) is 3.63×10^9 (Smith et al., 1975), a_g (for graupel) is 4.33×10^{10} (Gilmore et al., 2004). However, the coefficient is considered to be temperature dependent for snow: when the temperature is greater than 0°C, the coefficient for wet snow a_s is 4.26×10^{11}, while for dry snow, which occurs at temperature less than 0°C, a_s is 9.80×10^8 (Gunn and Marshall, 1958).

In the hydrometeor retrieval algorithm, q_x need to be calculated from a single measurement of Z_e. One of the important issues is to determine C_x, which is the ratio of each species' contribution to the total reflectivity. The component of reflectivity for each hydrometeor can then be partitioned by the following formula:

$$Z(q_x)=Z_e\cdot C_x. \tag{4}$$

Finally, substituting Eq. (4) into Eq. (3), the mixing ratio of each species can be obtained with

$$q_x=\exp\left(\ln\left(\frac{Z_e\cdot C_x}{a_x}\right)/1.75\right)/\rho. \tag{5}$$

As mentioned in the introduction, C_x in previous studies is generally based on the reflectivity (Z) and temperature (T); for convenience, this empirical Z and T based method is called HyRt-ZT. The HyRt-ZT method in the current WRFDA is employed in this study as a reference. In this scheme, the proportion of the snow and graupel is a fixed value that measured by the ratio of coefficients for snow and graupel, and the contribution of rainwater increases linearly from 0 to 1 between -5 °C to 5 °C (Gao and Stensrud, 2012).

2.3 Background dependent retrieval method

In fact, a fixed C_x is not appropriate for all areas and weather conditions. The composition of the hydrometeor field varies at different heights with different reflectivity values under different weather conditions. Therefore, we sought to build a hydrometeor retrieval method whose parameters update adaptively with the region and weather conditions in proportion to the contribution of each species from the background field.

First, for each hydrometeor type, we calculate the average reflectivity in the background field at different altitudes (z_i) and reflectivity intervals (ref_j) through

$$\overline{Z}_{x\,z_i,ref_j} = a_x \times (\overline{\rho}_{z_i,ref_j} \cdot \overline{q}_{x\,z_i,ref_j})^{1.75}, \tag{6}$$

where $\overline{\rho}_{z_i,ref_j}$ and $\overline{q}_{x\,z_i,ref_j}$ are the average air density and hydrometeor mixing ratios at grid points within the reflectivity interval (ref_j) at height z_i. In addition, the reflectivity intervals in this study areset as follows: ref_1: $<15dBZ$; ref_2: $15\sim25dBZ$; ref_3: $25\sim35dBZ$; ref_4: $35\sim45dBZ$; ref_5: $\geq 45dBZ$.

Then, Eq. (6) can be substituted into the following Eq. (7) to calculate the C_x in the background field:

$$C_{x(z_i,ref_j)} = \overline{Z}_{x\,z_i,ref_j} / \left(\overline{Z}_{r\,z_i,ref_j} + \overline{Z}_{s\,z_i,ref_j} + \overline{Z}_{g\,z_i,ref_j}\right). \tag{7}$$

where Z_r, Z_s and Z_g are the contributions to equivalent reflectivity Z_e by rainwater, snow, and graupel, respectively. After obtaining C_x from Eq. (7), the hydrometeor mixing ratios can be retrieved according to Eq. (5). Considering the possibility that the background may completely miss theconvection, a minimum number of grid points at which the reflectivity values are great than a threshold ref_j at height z_i is set to calculate

C_x. In this study, when the number is above 10, C_x is calculated using Eq. (7), otherwise a default value calculated from a one-month forecast climatology is used.

In addition, this study imposes a limitation on the retrieval process: only when there is strong convection at upper levels (i.e., reflectivity > 45dBZ, T<-5 ℃) can graupel appear below the melting layer. This method is called the "HyRt-BG" method hereafter.

3. Experimental design

3.1 Model configuration

The Advanced Research Weather Research and Forecasting model (ARW-WRF; Skamarock et al., 2008) V3.9.1 and its assimilation system WRFDA V3.9.1 are adopted in this study. The model is configured with two nested-grid domains at 9-km (D01) and 3-km horizontal grid spacings (D02) with 361×301 and 421×321 grid points, respectively (Fig. 1). Each domain features 41 vertical eta levels with a model top set at 50 hPa. The selected physical parameterization schemes mimic the operational settings used at the Meteorological Bureau of Shenzhen Municipality, China (Huang et al., 2018): the Thompson microphysical parameterization scheme (Thompson et al., 2008), Grell-Freitas cumulus parameterization scheme (Grell and Freitas, 2014), the Yonsei University PBL physics scheme (Hong et al., 2004), RRTMG longwave and shortwave radiation schemes (Iacono et al., 2008), and the Unified Noah land surface scheme (Tewari et al., 2004). The cumulus scheme is only activated on the coarser grid.

The National Meteorological Center (NMC) method (Parrish and Derber, 1992) is adopted to estimate the background error covariance. The statistical samples are the differences between 24 h and 12 h forecasts valid at the same time during a 1-month period from 15 April to 15 May, 2016. The selected control variables in this study are eastward and northward velocity components (U, V), surface pressure (P_s), temperature (T) and pseudo relative humidity (RH_s, water vapor mixing ratio divided by its saturated counterpart in the background field). U and V are selected as the momentum control variables to better assimilate radar radial velocity observations at convective scale (Sun et al., 2016; Shen et al., 2019). The hydrometeor control variables used in this study for reflectivity assimilation are rainwater, snow and graupel mixing ratios (Wang et al., 2013).

3.2 Setup of OSSEs

3.2.1 Truth Run and simulated observations

The truth simulation (referred to as the Truth Run hereafter) is used for generating simulated observations. In this study, a multi-cell storm in south China from 1200 UTC to 2000 UTC on 7 May 2017 was selected as the case of interest. Fig. 2 illustrates the schematic diagram of the OSSEs. First, the Truth Run is defined. The Truth Run is initialized at 0600 UTC, and the initial and lateral boundary conditions are provided by the 1°×1° NCEP final analysis (FNL) data. After a 6-hour spin-up process, conventional observations from the Global Telecommunication System (GTS) are assimilated in D01 and conventional data as well as radial velocity and reflectivity are assimilated in D02 beginning at 1200 UTC.An 8-hour forecast is then launched. The first hour forecast (at 1300 UTC) was discarded because the model variables were spinning up during this time period.

The forward operator for simulated radial velocity follows Xiao et al. (2005) and the forward operator for simulated reflectivity is given by Eqs. (2)-(3). The 3D wind field from the Truth Run is sampled by 7 pseudo-radars at 9 elevation angles (0.5°, 1.5°, 2.4°, 3.4°, 4.3°, 6.0°, 9.9°, 14.6° and 19.5°) corresponding to the operational WSR-88D scanning strategy VCP21 to obtain synthetic radial velocity data every hour from 1300 UTC to 2000 UTC. In contrast, the calculation of radar reflectivity is done on each model grid; no geometric transformation between radar observation space and model space is considered. This choice results in simulated observations that are as accurate as possible for evaluating of the retrieval method, and avoids interpolation errors of reflectivity introduced while converting between the model grid and the radar observation points.

3.2.2 Experiment design

First, the CTRL experiment was generated to provide the benchmark for the data assimilation experiments. In CTRL, the initial fields of D02 at 0600 UTC were interpolated from D01, and no radar data was assimilated. Then, three DA experiments, Exp-ZT, Exp-BG, and Exp-BG-Err, were performed to demonstrate the effectiveness of the background hydrometeor retrieval on short-term convective-scale weather forecasts (Fig. 2). In each DA experiment, the simulated radial velocity and reflectivity observations were assimilated hourly and a 3-hour forecast was then conducted in each cycle. The background fields at 1300 UTC were same as that of CTRL, while later they were provided by the 1-hour forecast from the previous cycle. In Exp-ZT, the WRFDA's default hydrometeor retrieval scheme (Wang et al., 2013) was employed, while the new proposed background-dependent hydrometeor retrieval scheme was adopted in Exp-BG. The third DA experiment, Exp-BG-Err, was carried out with a different microphysics scheme – the NSSL two-moment microphysics scheme (Mansell, 2010) – used in the WRF model forecast. The purpose of this experiment was to test the sensitivity of the background-dependent retrieval method to model errors. The retrievals, analyses and forecasts are then verified against the Truth Run to assess the accuracy of the retrieval and examine the impact of the retrieved hydrometeors on the analyses and forecasts.

4. Hydrometeor Retrievals

4.1 Hydrometeor distribution in background field

In this section, the retrieved hydrometeor mixing ratios (i.e., q_r, q_g, q_s) from the two different retrieval methods were compared to those from the Truth Run.

First, the evolution of the convection in the Truth Run is briefly described (Fig. 3). At 1300 UTC, a series of convective cells formed in the middle of the domain and two organized convective systems were present in the northeast part of the domain. By 1500 UTC, the cells in the middle of the domain intensified and became well organized, and the convection in the north weakened and moved out of the domain. By 1700 UTC, the systems had moved eastward and took on a linear structure. Finally, the systems gradually moved out of the Guangdong (GD) province and began to weaken and dissipate at 2000 UTC, while a strong convective system in the west was moving eastward.

In Exp-BG, the distributions of hydrometeors were first calculated from the background field. They were separated by model level and reflectivity interval in each analysis time, with the result at 1500 UTC shown in Fig. 4. The overall characteristics below 35 dBZ (Fig. 4a-c) are similar: the reflectivity below the 12th model level is mainly contributed from rainwater and above the 15th level is from dry snow; the contribution of wet snow near the melting layer increases gradually with increasing reflectivity threshold. For reflectivity larger than 45 dBZ (Fig. 4e), graupel accounts for a very large proportion, while dry snow accounts for less than 10% of the reflectivity. In the melting layer, the proportion of wet snow is the largest when the reflectivity is above 15 dBZ (Fig. 4b-e). Since it is from the same convective system, the distribution of C_x at other times is only slightly different (not shown). These results show that the contribution of each species varies appreciably in different reflectivity ranges and levels, indicating that a fixed threshold shouldn't be used for partitioning different reflectivity observations across hydrometeors even in the same weather regime.

4.2 Comparison of the retrieval results

The hydrometeor retrievals in the Exp-ZT, Exp-BG, and Exp-BG-Err at 1500 UTC and 1700 UTC were compared (Fig. 5). In Exp-ZT (Fig. 5b, f), the distributions of the retrieved snow and graupel are not reasonable because of the fixed proportions of snow and graupel adopted in HyRt-ZT scheme. In the area where a large quantity of snow should exist, the contribution to reflectivity was overly allocated to graupel, resulting in a great underestimation of snow in areas with high reflectivity values and an overestimation of graupel in areas with low reflectivity values. Great deviations of hydrometeors from Truth Run near the melting layer can also be seen in Exp-ZT, indicating that the fixed empirical rules cannot correctly partition the snow and graupel contributions in simulated reflectivity observations. This can induce large errors in the hydrometeor retrievals and their subsequent assimilation. In Exp-BG (Fig. 5c, g), however, even though some deviations can be seen in mixed-hydrometeor regions, the overall estimation of the three species is much closer to the Truth Run (Fig.5a, e). The improvement to the retrieval accuracy for the new scheme over the old one illustrates the importance of correctly partitioning the reflectivity for hydrometeor retrievals. However, the benefits of the new scheme may be overestimated in this experiment since model errors are not considered. Results from Exp-BG-Err show that the retrieval errors in are increased when adding model error, especially for graupel in upper levels (Fig.5d) and beneath the melting layer (Fig.5h), but the retrievals are still much closer to the Truth Run than that Exp-ZT. This demonstrates that the method can tolerate model errors to some degree.

To quantitatively evaluate the performance of the two methods, the bias and root mean square error (RMSE) were computed for the retrieved q_r, q_s and q_g from the HyRt-ZT, HyRt-BG, and HyRt-BG-Err respectively. Here the bias simply refers to the difference between the retrievals and the Truth. The bias and RMSE were computed at different mass mixing ratio thresholds (0.1, 0.3, 0.6, 1.0, 2.0, 5.0 g kg^{-1}) for the entire domain (D02) averaged over the whole duration of the simulation. For rainwater (Fig. 6a, d), the three experiments perform similarly, although HyRt-BG and HyRt-BG-Err slightly underestimated the rainwater when larger than 2 g kg^{-1} (about 10%). Snow is seriously underestimated in Exp-ZT (Fig. 6b, e), and the negative bias increases with the thresholds. The underestimation in Exp-ZT is more than 40% for greater than 2 g kg^{-1} and its RMSE is relatively high. This can be explained by the fixed proportion of reflectivity attributed to graupel in areas with high reflectivity values, which also leads to an overestimation of graupel in areas with the low reflectivity values. For graupel (Fig. 6c, f), besides the overestimation in areas with low reflectivity values, there is a similar underestimation in areas with large reflectivity values for HyRt-ZT (> 16%). The HyRt-BG has much smaller errors for both snow and graupel, which benefits from the successfully hydrometeor identification and reflectivity allocation. Considering model errors in Exp-BG-Err, the results of BIAS and RMSE for rain and snow become slightly worse than in Exp-BG (Fig. 6a, b, d, e), and for graupel, the retrieval errors increase a lot (Fig. 6c, f). So although the background hydrometeor retrieval method is slightly sensitive to model errors, the results still show some advantages over HyRt-ZT.

5. Short-term forecasts with the data assimilation of hydrometeor retrievals

5.1 Analysis and forecast of hydrometeors

To test the effects of the different hydrometeor retrieval methods on the short-term forecast of the MCS, the hydrometeor retrievals related to CTRL and three DA experiments HyRt-ZT, HyRt-BG and HyRt-BG-Err were assimilated into the model in one hour DA cycles, respectively, and three hour forecasts were launched every hour.

(1) Hydrometeor diagnostics

Fig. 7 shows the analysis fields of rain mixing ratio at about 2 km AGL and snow and graupel mixing ratios at about 6 km AGL at the time of the last analysis (1700 UTC) for the Truth Run and the three DA experiments. The differences for rain look very small because the retrieval processes are almost same in the three DA experiments (Fig. 7a-d). For Exp-ZT (Fig. 7j), the proportion of graupel is overestimated when the reflectivity values are; consequently, the snow is greatly underestimated (Fig. 7f). In comparison, snow is only slightly underestimated (Fig. 7g) while graupel looks reasonable (Fig. 7k) for Exp-BG. So benefit of proper partitioning of reflectivity information among different hydrometeors is clearly demonstrated in Exp-BG. Only small differences in the hydrometeor fields between Exp-BG (Fig. 7c, g, k) and Exp-BG-Err (Fig d, h, l) can be distinguished, indicating that the added model errors don’t appreciably impact the hydrometeors analysis at these levels. The vertical profiles of the analysis fields were also evaluated, with the conclusion quite similar to that of the horizontal analysis (not shown).

(2) 0-1h hydrometeor forecast

The hydrometeor fields in convection systems evolve rapidly and have low predictability (Fabry and Sun, 2010), so we first examine the impact of hydrometeor assimilation on the short-term forecast initiated at 1500 UTC.

At 15 min into the forecast, the ranges of rainwater, snow and graupel in both Exp-ZT and Exp-BG are closer to the Truth compared to the CTRL, which means that the data assimilation plays a positive role in the initial forecast (Fig. 8). But even if the vertical composite reflectivity for Exp-ZT and Exp-BG look similar (not shown), the internal structure of the hydrometeors are very different (Fig 8g, h, i, vs j, k, l). The simulation of rainwater, snow and graupel in the Exp-BG is much closer to the Truth Run. After 30 min into the forecast, the regions of nonzero hydrometeor fields in Exp-ZT become smaller than at 15 min. For the Exp-BG forecast, even though there is a slight deviation in position, the prediction of the convective cells overall is much better. At 60 min (Fig 8f, i, l), all three types of hydrometeors in Exp-ZT have dissipated more compared to the Truth Run, while Exp-BG performs the best. Comparing Exp-BG-Err with Exp-BG, snow above the melting level and rain below remain in good agreement, while less graupel and much more supercooled water exist due to the model integration using the NSSL two moment microphysics scheme.

Vertical cross sections of the temporal evolution of hydrometeors during the first 60 min are presented in Fig. 9. In the Truth Run, the content of all three types of hydrometeors gradually decreases with forecast time (Fig. 9a-c) because the convective system slowly moves out of the D02 domain. In general, the hydrometeor prediction in Exp-BG is the closest to the Truth Run. For rainwater, the difference between Exp-ZT and Exp-BG is not significant at the analysis time. However, a sharp increase in rainwater appears in Exp-ZT as soon as the model integration starts (Fig. 9g), which may be caused by the rapid melting and falling of graupel from upper levels (Fig. 9i). Snow is largely underestimated in Exp-ZT, and it is not until 30 min that the model produces relatively weaker snow prediction. In Exp-BG, in contrast, the benefit of the assimilation of retrieved snow is obvious in the first 30 min of the forecast (Fig. 9k). For graupel, Exp-BG has a more reasonable estimation at the initial time and the forecast (Fig. 9l), but Exp-ZT has an overestimation at the initial time and also overforecasts for the first 30 min. By adding model errors in Exp-BG-Err, rainwater and graupel weaken more quickly, while the evolution of snow is still very reasonable. Even though the advantages of HyRt-BG are diminished, the evolution of each hydrometeor in Exp-BG-Err is still closer to the truth run than that in Exp-ZT.

Despite the improvements in Exp-BG, the hydrometeors still dissipate rapidly and decrease by nearly half at 60 min, indicating that hydrometeors have a short duration without the updating or support of the related thermal and dynamic fields. The rate of dissipation of the hydrometeors is relatively slower in Exp-BG (see slope in Fig 9j-l), which may be due to the hydrometeor fields in Exp-BG being relatively more balanced with other model variables because they are derived from the background field.

5.2 Accumulated field and quantitative evaluation in the cycle

(1) 0-3h reflectivity forecast

Fig. 10 shows the simulated composite reflectivity fields from Truth Run, CTRL, Exp-ZT, Exp-BG, and Exp-BG-Err. These forecasts start at 1500 UTC in the middle of the cycle. In the simulated truth composite reflectivity fields (Fig. 10a, b, c), the MCSs are propagating southeastward slowly. Two major convective systems can be seen in Fig. 5a: one is in the center of the domain (labeled system A) and the other is in the northeast (labeled system B). In the CTRL, the prediction for system A is too weak, and system B is totally missed. In the two DA experiments, the region and intensity of both systems are substantially improved compared to the Exp-CTRL. One hour into the forecast (1600 UTC), the reflectivity core (system A) in Exp-ZT is weaker and narrower than Exp-BG, which may be caused by faster dissipation of the hydrometeors mentioned in section 4.2.2. By the second hour of the forecast (1700 UTC), the difference between Exp-ZT and Exp-BG is reduced, but Exp-BG still has broader and greater nonzero reflectivity coverage in system A, indicating that the convective systems in Exp-BG are more organized. After 3 hours, though better than CTRL, both Exp-ZT and Exp-BG lose the strength of the convection due to the hydrometeor dissipation. As we can see from Fig. 10m-o, adding model errors in Exp-BG-Err, the improvements brought by the background dependent retrieval method are still clear in 1h forecast, but not obvious after that. This may be because the differing microphysics scheme plays a significant role in the forecast over time.

(2) 0-3 h precipitation forecast

The quantitative precipitation forecast is an important indicator for evaluating the benefit brought by assimilation, so the hourly precipitation for each experiment is further evaluated. Fig. 11 shows the hourly accumulated precipitation of the last cycle for the Truth Run, CTRL, Exp-ZT, Exp-BG, and Exp-BG-Err. The precipitation is not well simulated by the CTRL (Fig. 11d-f), and the precipitation forecast is greatly improved after the retrieved hydrometeors are assimilated in Exp-ZT and Exp-BG experiments. During the first hour, both perform similarly (Fig. 11g, j). During the second hour, the regions of heavy rainfall (>15mm/h) in both Exp-ZT and Exp-BG (Fig. 11h, k) agree well with those in the Truth Run (Fig. 11b), and the Exp-BG performs much better. In the last hour, although the rainfall in Exp-ZT is much stronger than that of CTRL (Fig. 11f vs i), its intensity is still far less than the Truth Run. The Exp-BG performs the best among all experiments. For Exp-BG-Err, the rainfall is reasonable in the first hour forecast, but is weaker at later time compared with both Exp-ZT and Exp-BG due to mode errors.

To quantitatively evaluate the precipitation forecast of different experiments, the Fractions Skill Score (FSS, Roberts and Lean, 2008) at different thresholds are calculated against the Truth Run for each experiment. The FSS is more tolerant of small displacement errors and more suitable for precipitation evaluation with fine resolution grids (e.g., Fierro et al., 2015). In this study, the radius for FSS is about 15 km (5 neighborhood grid cells), and the evaluating area covers where the simulated reflectivity observations are greater than zero. The FSS of hourly accumulated precipitation with different thresholds (2.5, 5, and 15 mm) for CTRL, Exp-ZT, Exp-BG, and Exp-BG-Err are presented in Fig. 12. In general, the three DA experiments achieved higher FSS compared to CTRL at all thresholds in each forecast period. The more accurate analysis of the hydrometeor fields in Exp-BG resulted in the highest FSS at almost all thresholds compared with Exp-ZT except in the first hour and at lowest threshold (2.5 mm). During the first hour, the overall FSS in Exp-BG-Err at 2.5 and 5 mm is marginally the highest among all of the experiments, so the negative impact of model errors remains small for the first hour precipitation forecast. However, the model errors caused by a different microphysics scheme does reduce the forecast scores for 1-2 and 2-3 h forecasts. In general, Exp-BG performs better than Exp-ZT in most instances, even when including model error.

(3) RMSEs in the cycle

The average root-mean-square errors (RMSEs) of the CTRL, Exp-ZT, Exp-BG and Exp-BG-Err against the Truth Run over the 5 cycles are calculated for all three hydrometeor variables and water vapor (Fig. 13). At the analysis time (t=0), all three DA experiments have smaller errors of rain and snow than CTRL (Fig. 13a, b), while Exp-ZT has the largest errors for graupel because the reflectivity is wrongly attributed to graupel (Fig, 13c). The benefits of assimilating reflectivity decay rapidly in the first hour, and the differences in the hydrometeors between the DA experiments and CTRL narrow over time. The errors for snow in both Exp-BG and Exp-BG-Err (Fig. 13b) are the smallest over almost the entire 3-h time. This indicates that the well retrieved snow may last longer with the model integration. The assimilation of retrieved hydrometeors also helps improve the forecast of water vapor in Exp-BG, but with model errors included, it has a negative impact on the forecast of water vapor (Fig. 13d). Out of all three experiments, Exp-BG has the smallest forecast errors for water vapor, which may be a result of a more accurate analysis of hydrometeors in Exp-BG. The assimilation of retrieved hydrometeors may contribute to the gradual adjustment of other model fields like temperature, which leads to an improvement of the short-term precipitation forecast.

5.3 Diagnosis of temperature and moisture fields

In order to further identify the reason why the hydrometeor assimilation can improve the prediction beyond one hour, the temperature and moisture fields from the model and their response to the hydrometeors field are discussed below. To simplify the following discussion, Exp-BG-Err is not discussed.

Fig. 14 presents the vertical cross sections of temperature difference between each DA experiment and the Truth Run over the rainfall center from 24.2°N to 24.8°N in the last cycle. For the analysis, the differences in Exp-BG (Fig. 14d) are much smaller than those in Exp-ZT (Fig. 14a). In the 10-min forecast, the temperature in the middle levels in Exp-ZT becomes much colder than in Exp-BG because of the rapid melting of the ice particles, especially graupel. In the 3h forecast, the temperature differences of the two DA experiments narrows. But the Exp-BG still outperforms Exp-ZT in term of prediction of the MCS (between 114°E and 116°E). This leads to a better accumulated precipitation forecast in Exp-BG.

The relative humidity for the Truth Run, and the difference between the two DA experiments and the Truth Run over the rainfall center from 24.2°N to 24.8°N in the last cycle are shown in Fig. 15. At the analysis time, it is obvious that relative humidity in Exp-BG is closer to the truth than that in Exp-ZT. After 10 min of model integration, the melting and falling of graupel makes the upper-level air drier and the rapid increase of rain makes the lower-level air moister in the precipitation area (about 112°E~114°E) in Exp-ZT, while smaller differences can be seen in Exp-BG. After the 3-hour integration, the Exp-ZT and Exp-BG perform similarly, but an important improvement is that the moisture field between 850 hPa and 700 hPa ahead of the MCS (about 114°E ~116°E) has been enhanced in Exp-BG. Better humidity conditions in Exp-BG had a pronounced effect on the rainfall process.

This section shows that the impact of a better hydrometeor analysis on model forecast is primarily limited to the first hour. However, by cycling the analyses, the temperature and humidity fields are gradually influenced and the subsequent precipitation prediction is ultimately improved.

6. Conclusions

In this study, a background-dependent hydrometeor retrieval scheme was proposed to improve the accuracy of the hydrometer classification, analysis, and forecast. The main idea is to adaptively determine the contributions of the hydrometeors to the reflectivity according to the background field. The hydrometeor retrieval method was compared to the existing retrieval scheme in WRFDA through OSSEs.

The proportions of each hydrometeor species were calculated from the background fields and the accuracy of the retrieved hydrometeors from both schemes were first evaluated. It was found that the contribution of each hydrometeor species to the reflectivity varies widely in different reflectivity ranges and different vertical levels. This indicates that fixed parameters should not be used for calculating the contributions of each hydrometeor species to reflectivity even in the same background weather regime. By incorporating the background information, the retrieval reflectivity partitioning parameters became adaptive and the hydrometeor retrieval accuracy was greatly improved even when considering model error, especially in regions of mixed species.

The retrieved hydrometeors from both retrieval methods were then assimilated utilizing 3DVar with an hourly update cycling configuration. A better analysis of snow and graupel were obtained when the new retrieval method was used. Results show that both of the DA experiments improved the forecast of hydrometeors in the first hour, but the hydrometeors declined rapidly with the model integration. However, the additional data assimilation cycles helped the hydrometeors persist in Exp-BG. The reason for these improvements may be that Exp-BG implicitly included the model constraints, and thus the retrieved hydrometeor fields are relatively more balanced with other model variables.

The improvement of the hydrometeors' forecast in this study was mainly concentrated within the first hour, but with the hourly update cycling configuration, it further affected other variables like temperature and humidity through thermodynamic and microphysical processes. The improvement of the temperature and humidity fields was achieved and had a pronounced effect on the rainfall processes, so that the assimilation of retrieved hydrometeors ultimately improved the short-term forecast of reflectivity and precipitation.

Though our proposed scheme shows promising results, problems still exist. First, the improvement of hydrometeor fields has a relatively short duration, which can be improved by considering multivariate correlation among hydrometeors and other analysis variables in the static background error or introducing a flow-dependent background error through a variational-ensemble hybrid method (Pan et al., 2018; Meng et al. 2019). Second, due to the lack of real observations of sufficiently high spatial and temporal resolution, the new scheme was only evaluated through OSSEs. Although its value has been proved, further testing is also needed using real data cases. Finally, dual-polarization radar data are an important additional source of information for classification of hydrometeors beyond Z, so it is likely that better retrievals and forecasts can be achieved with the assistance of polarimetric information.

Acknowledgements

This work was jointly sponsored by the National Key Research and Development Program of China (2017YFC1502102) and National Natural Science Foundation of China (41675102), the Special Fund for Meteorological Scientific Research in Public Interest (GYHY201506002). The GFS analysis and the conventional observations are obtained from Data Support Section of the Computational and Information Systems Laboratory at the National Center for Atmospheric Research in Boulder (http://dss.ucar.edu/datasets). The radar observations are provided by the Numerical Weather Prediction Center of CMA (China Meteorological Administration).

Reference

1. Barker, D., Huang, X., Liu, Z., Auligné, T., Zhang, X., Rugg, S., Ajjaji, R.,

Bourgeois, A., Bray, J., Chen, Y., Guo, Y., Henderson, T., Huang, W., Lin. H., Michalakes, J., Rizvi, S., Zhang, X., 2012. The Weather Research and Forecasting Model's Community Variational/Ensemble Data Assimilation System: WRFDA. Bulletin of the American Meteorological Society, 93, 831-843. https://doi.org/10.1175/BAMS-D-11-00167.1

2. Bauer, P., Auligné, T., Bell, W., Geer, A., Guidard, V., Heilliette, S., Kazumori, M., Kim, M., Liu, E. H., McNally, A. P., Macpherson, B., Okamoto, K., Renshaw, R., Riishøjgaard, L., 2011. Satellite cloud and precipitation assimilation at operational NWP centres. Quarterly Journal of the Royal Meteorological Society, 137, 1934-1951. https://doi.org/10.1002/qj.905
3. Carlin, J. T., Ryzhkov, A. V., Snyder, J.C., Khain, A., 2016. Hydrometeor Mixing Ratio Retrievals for Storm-Scale Radar Data Assimilation: Utility of Current Relations and Potential Benefits of Polarimetry. Monthly Weather Review, 144, 2981-3001. https://doi.org/10.1175/MWR-D-15-0423.1
4. Caumont, O., Ducrocq, V., Wattrelot, É., Jaubert, G., Pradier-Vabre, S., 2010. 1D+3DVar assimilation of radar reflectivity data: a proof of concept. Tellus, Series A, 62, 173-187. https://doi:10.1111/j.1600-0870.2009.00430.x
5. Chang, S., Liou, Y., Sun, J., Tai, S., 2016. The Implementation of the Ice-PhaseMicrophysical Process into a Four-Dimensional Variational Doppler Radar Analysis System (VDRAS) and Its Impact on Parameter Retrieval and Quantitative Precipitation Nowcasting. Journal of Atmospheric Sciences, 73, 1015–1038. https://doi.org/10.1175/JAS-D-15-0184.1
6. Fabry, F., Sun, J., 2010. For How Long Should What Data Be Assimilated for the Mesoscale Forecasting of Convection and Why? Part I: On the Propagation of Initial Condition Errors and Their Implications for Data Assimilation. Monthly Weather Review, 138, 242-255. https://doi.org/10.1175/2009MWR2883.1
7. Fierro, A. O., Clark, A. J., Mansell, E. R., MacGorman, D. R., Dembek, S. R., Ziegler, C. L., 2015. Impact of Storm-Scale Lightning Data Assimilation on WRF-ARW Precipitation Forecasts during the 2013 Warm Season over the Contiguous United States. Monthly Weather Review, 143, 757-777. https://doi.org/10.1175/MWR-D-14-00183.1
8. Gao, J., Stensrud, G. G., Xue, M., 2009. The relative importance of assimilating radial velocity and reflectivity data. Abstract extended at 23nd Conference on Weather Analysis and Forecasting/19th Conference on Numerical Weather Prediction, Omaha, NB, Amer. Meteor. Soc., 8A.1.
9. Gao, J., Xue, M., Droegemeier, K. K., 2004. A three-dimensional variational data analysis method with recursive filter for Doppler radars. Journal of Atmospheric Oceanic Technology, 21, 457-469. https://doi.org/10.1175/1520-0426(2004)021<0457:ATVDAM>2.0.CO;2
10. Gao, J., Stensrud, G. G., 2012. Assimilation of Reflectivity Data in a Convective-Scale, Cycled 3DVAR Framework with Hydrometeor Classification. Journal of Atmospheric Sciences, 69, 1054-1065. https://doi.org/10.1175/JAS-D-11-0162.1
11. Gilmore, M. S., Straka, J. M., Rasmussen, E. N., 2004. Precipitation and Evolution Sensitivity in Simulated Deep Convective Storms: Comparisons between Liquid-

Only and Simple Ice and Liquid Phase Microphysics. Monthly Weather Review, 132, 1897–1916. https://doi.org/10.1175/1520-0493(2004)132<1897:PAESIS>2.0.CO;2

12. Grell, G. A., Freitas, S. R., 2014. A scale and aerosol aware stochastic convective parameterization for weather and air quality modeling. Atmospheric Chemistry and Physics, 14, 5233-5250. https://doi.org/10.5194/acp-14-5233-2014
13. Gunn, K. L. S., Marshall, J. S., 1958. The distribution with size of aggregate snowflakes. Journal of Meteorology, 15(5), 452-461. https://doi.org/10.1175/1520-0469(1958)015<0452:TDWSOA>2.0.CO;2
14. Hong, S. Y., Dudhia, J., Chen, S. H., 2004. A revised approach to ice microphysical processes for the bulk parameterization of clouds and precipitation. Monthly Weather Review, 132, 103-120. https://doi.org/10.1175/1520-0493(2004)132<0103:ARATIM>2.0.CO;2
15. Hu, M., Xue, M., Gao, J., Brewster, K., 2006. 3DVAR and cloud analysis with WSR-88D level-II data for the prediction of the Fort Worth, Texas, tornadic thunderstorms. Part II: Impact of radial velocity analysis via 3DVAR, Monthly Weather Review, 134, 699-721. https://doi.org/10.1175/MWR3093.1
16. Huang, Y., Liu, Y., Xu, M., Liu, Y., Pan, L., Wang, H., Cheng, W. Y.Y., Jiang, Y., Lan, H., Yang, H., Wei, X., Zong, R., Cao, C., 2018. Forecasting severe convective storms with WRF-based RTFDDA radar data assimilation in Guangdong, China. Atmospheric Research, 209, 131-143. https://doi.org/10.1016/j.atmosres.2018.03.010
17. Mansell, E.R., C.L. Ziegler, and E.C. Bruning, 2010: Simulated Electrification of a Small Thunderstorm with Two-Moment Bulk Microphysics. J. Atmos. Sci., 67, 171–194, https://doi.org/10.1175/2009JAS2965.1
18. Iacono, M. J., Delamere, J. S., Mlawer, E. J., Shephard, M. W., Clough, S. A., Collins, W. D., 2008. Radiative forcing by long-lived greenhouse gases: Calculations with the AER radiative transfer models, Journal of Geophysical Research: Atmospheres, 113, D13103, https://doi.org/10.1029/2008JD009944.
19. Jung, Y., Zhang, G., Xue, M., 2008. Assimilation of Simulated Polarimetric Radar Data for a Convective Storm Using the Ensemble Kalman Filter. Part I: Observation Operators for Reflectivity and Polarimetric Variables. Monthly Weather Review, 136, 2228–2245, https://doi.org/10.1175/2007MWR2083.1
20. Kerr, C. A., Stensrud, D. J., Wang, X., 2015. Assimilation of cloud top temperature and radar observations of an idealized splitting supercell using an Observing System Simulation Experiment. Monthly Weather Review, 143, 1018–1034, https://doi.org/10.1175/MWR-D-14-00146.1
21. Lai, A., Gao, J., Koch, S., Wang, Y., Pan, S., Fierro, A. O., Cui, C., Min. J., 2019. Assimilation of Radar Radial Velocity, Reflectivity, and Pseudo–Water Vapor for Convective-Scale NWP in a Variational Framework. Monthly Weather Review, 147, 2877-2900. https://doi.org/10.1175/MWR-D-18-0403.1
22. Lerach, D.G., Rutledge, S.A., Williams, C.R., Cifelli, R., 2010. Vertical structure of convective systems during NAME 2004. Monthly Weather Review, 138, 1695–1714. https://doi.org/10.1175/2009MWR3053.1

23. Lilly, D. K., 1990. Numerical prediction of thunderstorms—has its time come? Quarterly Journal of the Royal Meteorological Society, 116, 779-798. https://doi.org/10.1002/qj.49711649402
24. Liu, C., Xue, M., Kong, R., 2019. Direct Assimilation of Radar Reflectivity Data using 3DVAR: Treatment of Hydrometeor Background Errors and OSSE Tests. Monthly Weather Review, 147, 17–29. https://doi.org/10.1175/MWR-D-18-0033.1
25. Lopez, P. Bauer, P., 2007. "1D+4DVAR" Assimilation of NCEP Stage-IV Radar and Gauge Hourly Precipitation Data at ECMWF. Monthly Weather Review, 135, 2506–2524, https://doi.org/10.1175/MWR3409.1
26. Matsui, T., Dolan, B., Rutledge, S. A., Tao, W. K., Iguchi, T., Barnum, J., Lang, S. E., 2019. POLARRIS: A POLArimetric Radar Retrieval and Instrument Simulator. Journal of Geophysical Research: Atmospheres, 124(8), 4634-4657. https://doi.org/10.1029/2018JD028317
27. Meng, D., Chen, Y. Wang, H., Gao, Y., Potthast, R., Wang, Y., 2019. The evaluation of EnVar method including hydrometeors analysis variables for assimilating cloud liquid/ice water path on prediction of rainfall events. Atmosphere Research, 219, 1–12. https://doi.org/10.1016/j.atmosres.2018.12.017
28. Pan, S., Gao, J., Stensrud, D. J., Wang, X., Jones, T. A., 2018. Assimilation of Radar Radial Velocity and Reflectivity, Satellite Cloud Water Path, and Total Precipitable Water for Convective-Scale NWP in OSSEs. Journal of Atmospheric and Oceanic Technology, 35, 67–89. https://doi.org/10.1175/JTECH-D-17-0081.1
29. Pan, Y., Xue, M., Ge, G., 2016. Incorporating diagnosed intercept parameters and the graupel category within the ARPS cloud analysis system for the initialization of double-moment microphysics: Testing with a squall line over south China. Monthly Weather Review, 144, 371–392. https://doi.org/10.1175/MWR-D-15-0008.1
30. Pan, Y., Wang, M., 2018. Impact of assimilation frequency of radar data with ARPS 3DVar and Cloud Analysis System on forecasts of a squall line in southern China. Advances in Atmospheric Sciences, 36(2), 160-172. https://doi.org/10.1007/s00376-018-8087-5
31. Parrish, D.F., J.C. Derber., 1992. The National Meteorological Center's Spectral Statistical-Interpolation Analysis System. Monthly Weather Review, 120, 1747–1763. https://doi.org/10.1175/1520-0493(1992)120<1747:TNMCSS>2.0.CO;2
32. Putnam, B., Xue, M., Jung, Y., Snook, N., Zhang, G., 2019. Ensemble Kalman Filter Assimilation of Polarimetric Radar Observations for the 20 May 2013 Oklahoma Tornadic Supercell Case. Monthly Weather Review, 147, 2511–2533. https://doi.org/10.1175/MWR-D-18-0251.1
33. Roberts, N.M. Lean, H.W., 2008. Scale-Selective Verification of Rainfall Accumulations from High-Resolution Forecasts of Convective Events. Monthly Weather Review, 136, 78–97. https://doi.org/10.1175/2007MWR2123.1
34. Skamarock, W. C., Klemp, J. B., 2008. A time-split nonhydrostatic atmospheric model for weather research and forecasting applications. Journal of computational physics, 227, 3465–3485. https://doi.org/10.1016/j.jcp.2007.01.037
35. Smith, P. L., Myers, C. G., Orville, H. D., 1975. Radar Reflectivity Factor Ca lculations in Numerical Cloud Models Using Bulk Parameterization of Precipit

ation. Journal of Applied Meteorology, 14, 1156–1165. https://doi.org/10.1175/1520-0450(1975)014<1156:RRFCIN>2.0.CO;2

36. Sugimoto, S., Crook, N.A., Sun, J., Xiao, Q., Barker, D.M., 2009. An Examination of WRF 3DVAR Radar Data Assimilation on Its Capability in Retrieving Unobserved Variables and Forecasting Precipitation through Observing System Simulation Experiments. Monthly Weather Review, 137, 4011–4029, https://doi.org/10.1175/2009MWR2839.1
37. Sun, J., Wang, H., Tong, W., Zhang, Y., Lin, C., Xu, D., 2016. Comparison of the Impacts of Momentum Control Variables on High-Resolution Variational Data Assimilation and Precipitation Forecasting. Monthly Weather Review, 144, 149–169, https://doi.org/10.1175/MWR-D-14-00205.1
38. Sun, J., Crook, N.A., 1997. Dynamical and Microphysical Retrieval from Doppler Radar Observations Using a Cloud Model and Its Adjoint. Part I: Model Development and Simulated Data Experiments. Journal of Atmospheric Sciences, 54, 1642–1661. https://doi.org/10.1175/1520-0469(1997)054<1642:DAMRFD>2.0.CO;2
39. Sun, J., Crook, A. N., 1998. Dynamical and microphysical retrieval from Doppler radar observations using a cloud model and its adjoint. Part II: Retrieval experiments of an observed Florida convective storm. Journal of Atmospheric Sciences, 55, 835–852. https://doi.org/10.1175/1520-0469(1998)055<0835:DAMRFD>2.0.CO;2
40. Sun, J., Xue, M., Wilson, J. W., Zawadzki, I., Ballard, S. P., Onvlee-Hooimeyer J., Joe, P., Barker, D. M., Li, P., Golding, B., Xu, M., Pinto, J., 2014. Use of NWP for Nowcasting Convective Precipitation: Recent Progress and Challenges. Bulletin of the American Meteorological Society, 95, 409–426, https://doi.org/10.1175/BAMS-D-11-00263.1
41. Tewari, M., Chen, F.,Wang W., Dudhia, J., LeMone, M. A., Mitchell, K., Gayno, M. Ek. G., Wegiel, J., Cuenca, R. H., 2004. Implementation and verification of the unified NOAH land surface model in the WRF model, 20th Conference on Weather analysis and Forecasting/16th Conference on Numerical Weather Prediction, pp. 11–15.
42. Thompson, G., Field, P. R., Rasmussen, R. M., Hall, W.D., 2008. Explicit Forecasts of Winter Precipitation Using an Improved Bulk Microphysics Scheme. Part II: Implementation of a New Snow Parameterization. Monthly Weather Review, 136, 5095–5115, https://doi.org/10.1175/2008MWR2387.1
43. Tong, M., Xue, M., 2005. Ensemble Kalman Filter Assimilation of Doppler Radar Data with a Compressible Nonhydrostatic Model: OSS Experiments. Monthly Weather Review, 133, 1789–1807, https://doi.org/10.1175/MWR2898.1
44. Wang, H., Liu, Y., Zhao, T., Xu, M., Liu Y., Guo, F., Cheng, W. Y.Y., Feng, S., Mansell, E. R., Fierro, A. O., 2018. Incorporating geostationary lightning data into a radar reflectivity based hydrometeor retrieval method: An observing system simulation experiment. Atmospheric Research, 209, 1-13. https://doi.org/10.1016/j.atmosres.2018.03.002
45. Wang, H., Sun, J., Fan S., Huang, X., 2013. Indirect assimilation of radar

reflectivity with WRF 3D-Var and its impact on prediction of four summertime convective events. Journal of Applied Meteorology and Climatology, 52, 889-902. https://doi.org/10.1175/JAMC-D-12-0120.1

46. Wang, S., Liu, Z., 2019. A radar reflectivity operator with ice-phase hydrometeors for variational data assimilation (version 1.0) and its evaluation with real radar data, Geoscientific Model Development, 12, 4031–4051. https://doi.org/10.5194/gmd-12-4031-2019
47. Wu, B., Verlinde, J., Sun, J., 2000. Dynamical and Microphysical Retrievals from Doppler Radar Observations of a Deep Convective Cloud. Journal of Atmospheric Sciences, 57, 262–283. https://doi.org/10.1175/1520-0469(2000)057<0262:DAMRFD>2.0.CO;2
48. Xiao, Q., Kuo, Y., Sun, J., Lee, W., Lim, E., Guo, Y., Barker, D. M., 2005. Assimilation of Doppler Radar Observations with a Regional 3DVAR System: Impact of Doppler Velocities on Forecasts of a Heavy Rainfall Case. Journal of Applied Meteorology, 44, 768–788. https://doi.org/10.1175/JAM2248.1
49. Xiao, Q., Kuo, Y., Sun, J., Lee, W., Barker, D. M., Lim, E., 2007. An Approach of Radar Reflectivity Data Assimilation and Its Assessment with the Inland QPF of Typhoon Rusa (2002) at Landfall. Journal of Applied Meteorology and Climatology, 46, 14–22, https://doi.org/10.1175/JAM2439.1
50. Yokota, S., Seko, H., Kunii, M., Yamauchi, H., Niino, H., 2016. The Tornadic Supercell on the Kanto Plain on 6 May 2012: Polarimetric Radar and Surface Data Assimilation with EnKF and Ensemble-Based Sensitivity Analysis. Monthly Weather Review, 144, 3133–3157, https://doi.org/10.1175/MWR-D-15-0365.1
51. Zhang, G., Mahale, V. M., Putnam, B. J., Qi, Y., Cao, Q., Byrd, A. D., Bukovcic P., Zrnic D. S., Gao, J., Xue, M., Jung, Y., Reeves, H. D., Heinselman, P. L., Ryzhkov, A., Palmer, R. D., Zhang, P., Weber, M., Mcfarquhar, G. M., Moore III, B., Zhang, Y., Zhang, J., Vivekanandan, J., Al-Rashid, Y., Berkowitz, D. S., Tong. C., Fulton, C., Doviak, R. J., 2019. Current Status and Future Challenges of Weather Radar Polarimetry: Bridging the Gap between Radar Meteorology/Hydrology/Engineering and Numerical Weather Prediction. Advances in Atmospheric Sciences, 36(6):571-588. https://doi.org/10.1007/s00376-019-8172-4
52. Zrnić, D.S., Ryzhkov, A., Straka, J., Liu, Y., Vivekanandan J., 2001. Testing a Procedure for Automatic Classification of Hydrometeor Types. Journal of Atmospheric and Oceanic Technology, 18, 892–913, https://doi.org/10.1175/1520-0426(2001)018<0892:TAPFAC>2.0.CO;2

Figure captions

Fig. 1. Domain size and radars used in the study. The range for each radar is shown roughly by the blue circle.

Fig. 2. Schematic diagram showing the assimilation and forecast cycles in the OSSEs.

Fig. 3. Composite radar reflectivity fields of the Truth Run in domain D02. The valid forecast time is shown above each panel. The black lines in (b) and (d) indicate the locations of the vertical cross sections shown in Fig. 5 and 6. The small blue box in (b) indicates the hydrometeor calculation region in Fig. 9.

Fig. 4. The vertical profiles of each hydrometeor's contribution to the total reflectivity in different reflectivity ranges at 1500 UTC. (A)- (e) shows the distribution of C_x with height in different reflectivity intervals, where $ref_1\!: < 15dBZ; ref_2\!: 15 \sim 25dBZ; ref_3\!: 25 \sim 35dBZ;\ ref_4\!: 35 \sim 45dBZ;\ ref_5\!: \geq 45dBZ$.

Fig. 5. Vertical cross-sections of the hydrometeor mixing ratio fields: q_g (color shading), q_s (blue contours), q_r (green contours) from (a), (e) Truth Run; (b), (f) Exp-ZT; (c), (g) Exp-BG; (d), (h) Exp-BG-Err. Legend for the color shadings for q_g (g kg^{-1}) is shown on the bottom. The contour intervals of q_s (g kg^{-1}) are 0.1, 0.2, 0.5, 1.0, 2.5. The contour intervals of q_r (g kg^{-1}) are 0.01, 0.1, 0.2, 0.5, 1.0. The locations of the vertical cross sections are denoted by the black lines in Fig. 3. (A)-(d) is valid at 1500 UTC and (e)-(h) is valid at 1700 UTC. The dashed black line indicates where the temperature is 0°C.

Fig. 6. The average bias (top) and root mean square error (RMSE; bottom) at different thresholds for the retrievals of (a, d) q_r; (b, e) q_s; (c, f) q_g for Exp-ZT (blue solid line), Exp-BG (red solid line) and Exp-BG-Err (red dashed line) relative to the Truth Run over the whole cycle.

Fig. 7. Analysis of (a-d) rain at about 2km AGL, (e-h) snow and (i-l) graupel mixing ratio at about 6km AGL. (a), (e), (i) is the analysis for Truth Run, (b), (f), (j) is for Exp-ZT, (c), (g), (k) is for Exp-BG and (d), (h), (l) is for Exp-BG-Err. The analysis time is 1700 UTC.

Fig. 8. Vertical cross-sections of the hydrometeor mixing ratio fields: q_g (color shading), q_s (blue contours), q_r (green contours) from (a-c) Truth; (d-f) CTRL; (g-i) Exp-ZT; (j-l) Exp-BG and (m-o) Exp-BG-Err. Legend for the color shadings for q_g (g kg^{-1}) is shown on the bottom. The contour intervals of q_s (g kg^{-1}) are 0.1, 0.2, 0.5, 1.0, 2.5. The contour intervals of q_r (g kg^{-1}) are 0.01, 0.1, 0.2, 0.5, 1.0. The three columns represent the 15, 30 and 60 min forecasts initialized at 1500 UTC, respectively. The locations of the vertical cross sections are shown in line AB in Fig. 3.

Fig. 9. Vertical cross sections of the temporal evolution of horizontally-averaged hydrometeor mixing ratios in the first 60 minutes over the convective center (units: g kg^{-1}) of (a-c) Truth Run; (d-f) CTRL; (g-i) Exp-ZT; (j-l) Exp-BG; and (m-o) Exp-BG-Err. The forecasts are initiated at 1500 UTC. The calculation region is denoted by the blue box in Fig. 3.

Fig. 10. Composite reflectivity forecasts initialized at 1500 UTC from (a-c) Truth; (d-f) CTRL; (g-i) Exp-ZT, (j-l) Exp-BG and (m-o) Exp-BG-Err. The three columns represent the 1-hour forecast, 2-hour forecast and 3-hour forecasts, respectively.

Fig. 11. Hourly accumulated precipitation rates (mm) of the last cycle for (a-c) Truth, (d-f) CTRL, (g-i) Exp-ZT, and (j-l) Exp-BG, and (m-o) Exp-BG-Err. The three columns represent the accumulated precipitation during the first hour, second hour and third hour's forecast, respectively. The red frame indicates the diagnosed region in Fig. 14 and 15.

Fig. 12. Averaged Fractions Skill Scores of the hourly-accumulated precipitation forecasts for thresholds of 2.5 mm, 5 mm and 15 mm for CTRL, Exp-ZT, Exp-BG and Exp-BG-Err over the whole cycle. The radius of influence of the neighborhood method used in this study is about 15 km and the scoring area covers the entire precipitation area in Fig. 11.

Fig. 13. Time series of the analysis and forecast RMSEs of (a) q_r at 850hPa, (b) q_s at 400hPa, (c) q_g at 300hPa and (d) q_v at 700hPa for the whole cycle.

Fig. 14. Cross sections of temperature fields (shaded; K) for (a-c) the difference between Exp-ZT and the Truth Run and (d-f) the difference between Exp-ZT and the Truth Run over the rainfall center from 24.2°N to 24.8°N. The rainfall center is denoted by the red frame in Fig. 11(f). (a, d) are the analyses valid at 1700 UTC. (b, e) are the 10-min forecasts initiated at 1700UTC. (c, f) are the 3-hour forecasts initiated at 1700 UTC.

Fig 15. Cross sections of relative humidity fields (shaded; %) for (a-c) Truth, (d-f) the difference between Exp-ZT and the Truth Run, and (g-i) the difference between Exp-BG and the Truth Run over the rainfall center from 24.2°N to 24.8°N. The rainfall center is denoted by the red frame in Fig. 11(f). (a, d, g) are the analyses valid at 1700 UTC. (b, e, h) are the 10-min forecasts initiated at 1700 UTC. (c, f, i) are the 3-hour forecasts initiated at 1700 UTC.

Figures

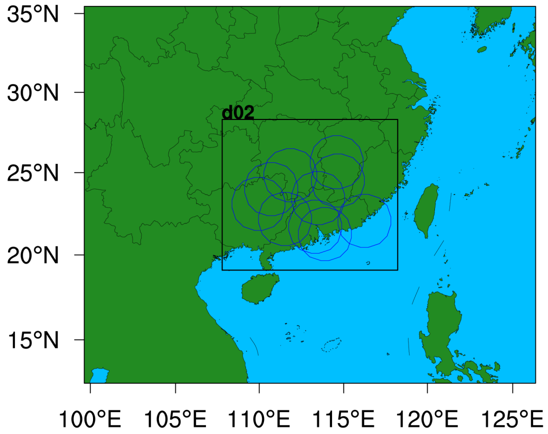

Fig. 1. Domain size and radars used in the study. The range for each radar is shown roughly by the blue circle.

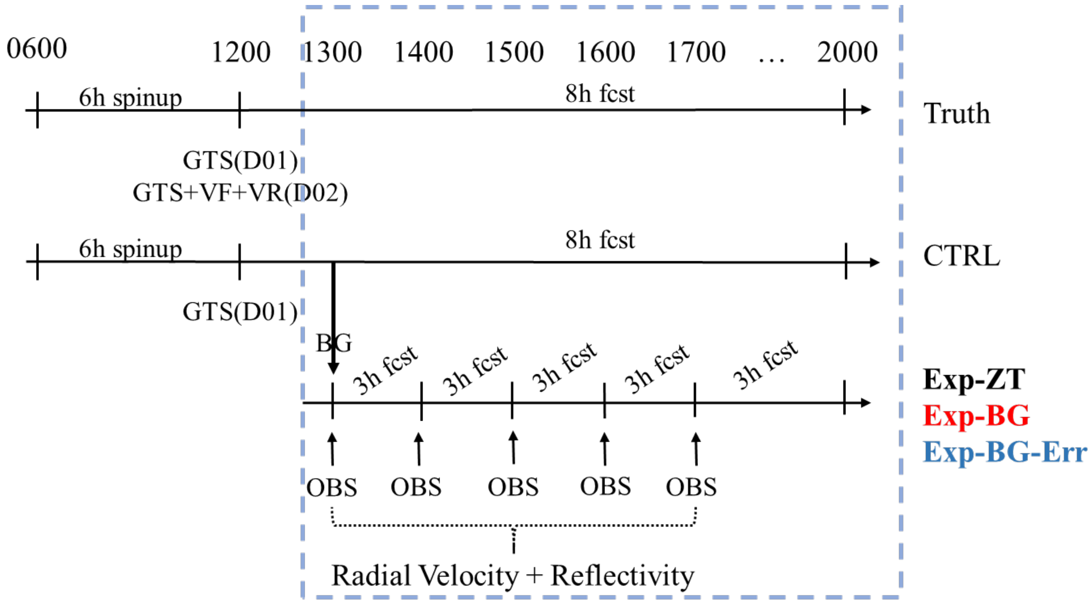

Fig. 2. Schematic diagram showing the assimilation and forecast cycles in the OSSEs.

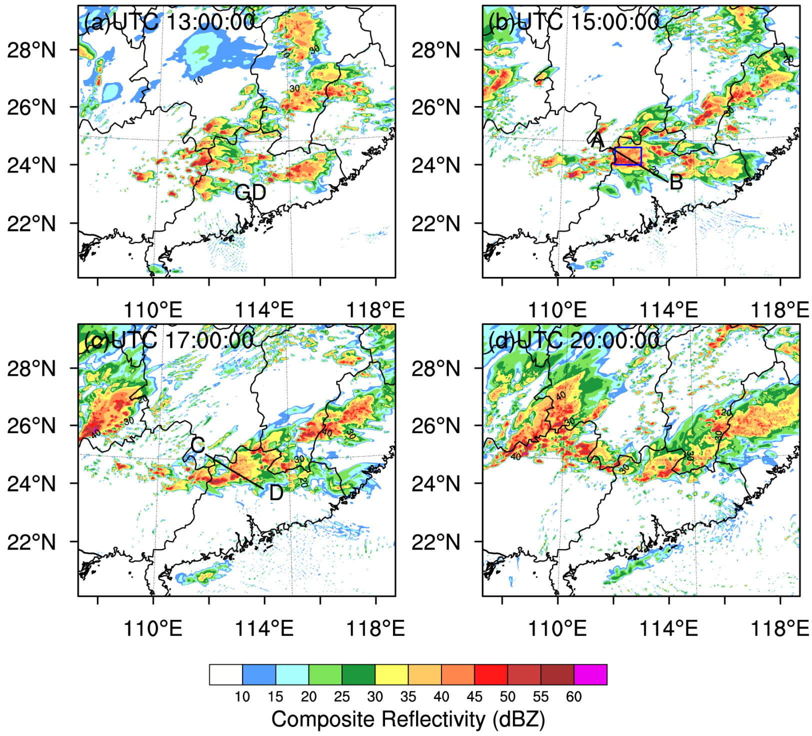

Fig. 3. Composite radar reflectivity fields of the truth simulation in domain D02. The valid forecast time is shown above each panel. The black lines in (b) and (d) indicate the locations of the vertical cross sections shown in Fig. 5 and 6. The small blue box in (b) indicates the hydrometeor calculation region in Fig. 9.

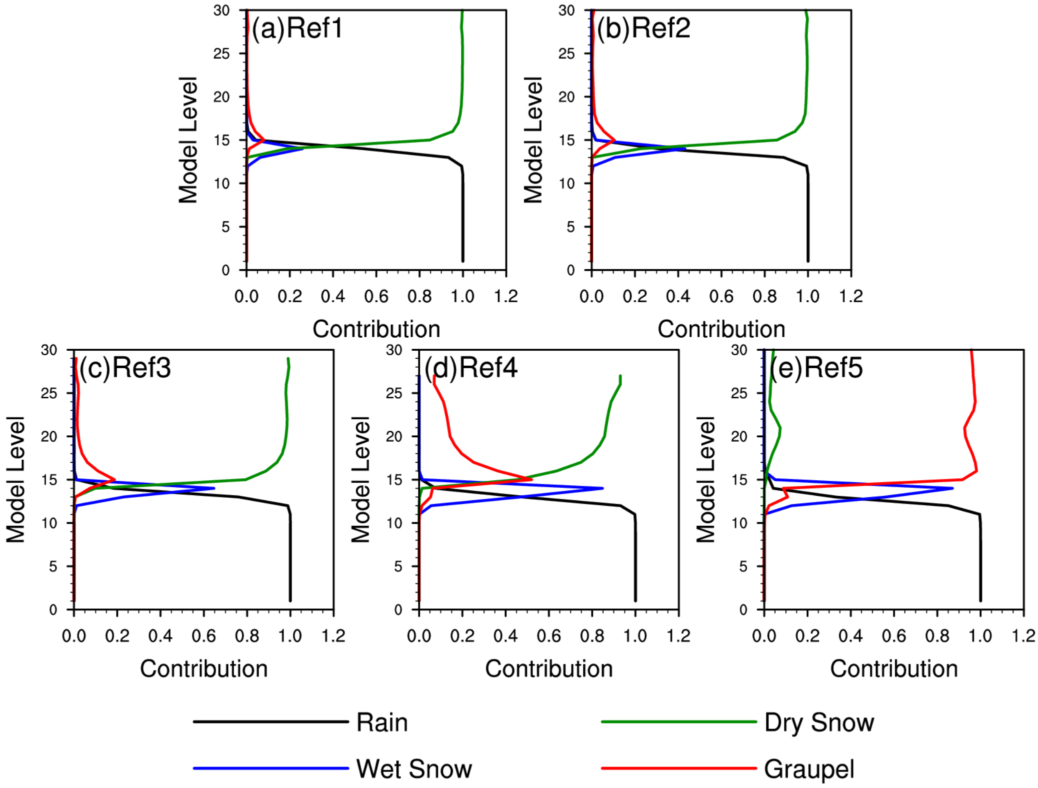

Fig. 4. The vertical profiles of the each hydrometeor's contribution to the total reflectivity in different reflectivity ranges at 1500 UTC. (A)- (e) shows the distribution of C_x with height in different reflectivity intervals, where ref_1: $< 15dBZ$; ref_2: $15\sim25dBZ$; ref_3: $25\sim35dBZ$; ref_4: $35\sim45dBZ$; ref_5: $\geq 45dBZ$.

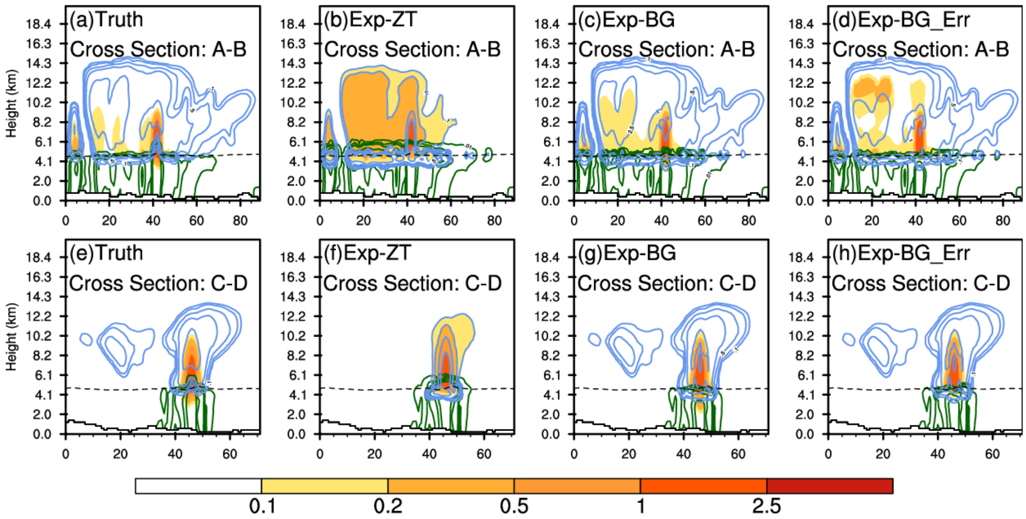

Fig. 5. Vertical cross-sections of the hydrometeor mixing ratio fields: q_g (color shading), q_s (blue contours), q_r (green contours) from (a), (e) Truth Run; (b), (f) Exp-ZT; (c), (g) Exp-BG; (d), (h) Exp-BG-Err. Legend for the color shadings for q_g (g kg^{-1}) is shown on the bottom. The contour intervals of q_s (g kg^{-1}) are 0.1, 0.2, 0.5, 1.0, 2.5. The contour intervals of q_r (g kg^{-1}) are 0.01, 0.1, 0.2, 0.5, 1.0. The locations of the vertical cross sections are denoted by the black lines in Fig. 3. (A)-(d) is valid at 1500 UTC and (e)-(h) is valid at 1700 UTC. The dashed black line indicates where the temperature is 0°C.

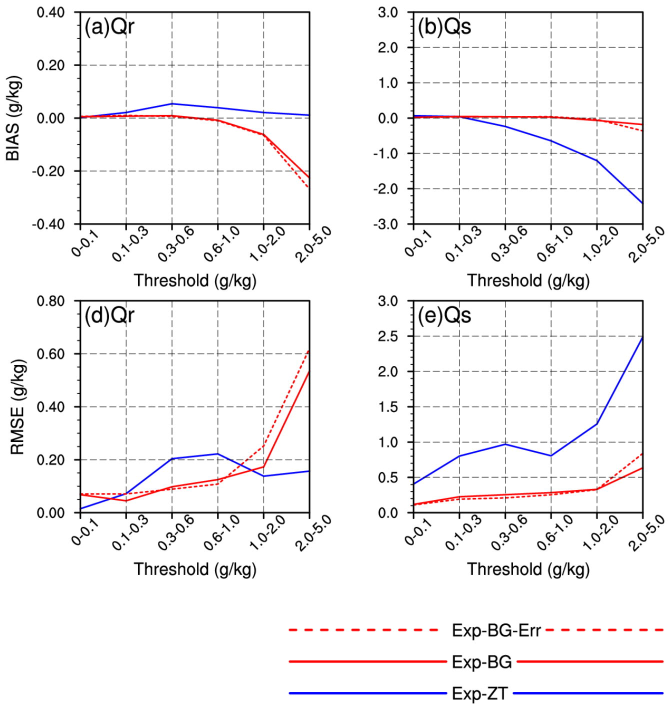

Fig. 6. The average bias (top) and root mean square error (RMSE; bottom) at different thresholds for the retrievals of (a, d) q_r; (b, e) q_s; (c, f) q_g for Exp-ZT (blue solid line), Exp-BG (red solid line) and Exp-BG-Err (red dashed line) relative to the true simulation over the whole cycle.

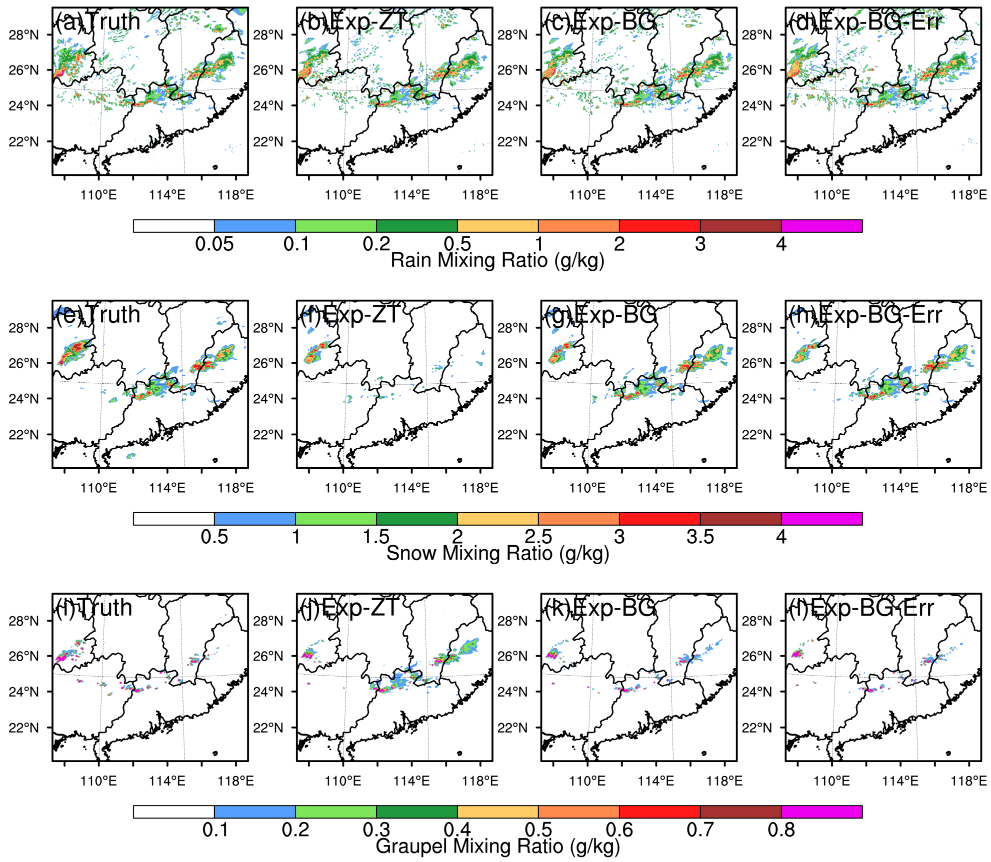

Fig. 7. Analysis of (a-c) rain at about 2km AGL, (d-f) snow and (g-i) graupel mixing ratio at about 6km AGL. (a), (d), (g) is the analysis for Truth Run, (b), (e), (h) is for Exp-ZT, (c), (f), (i) is for Exp-BG and (d), (h), (l) is for Exp-BG. The analysis time is 1700 UTC.

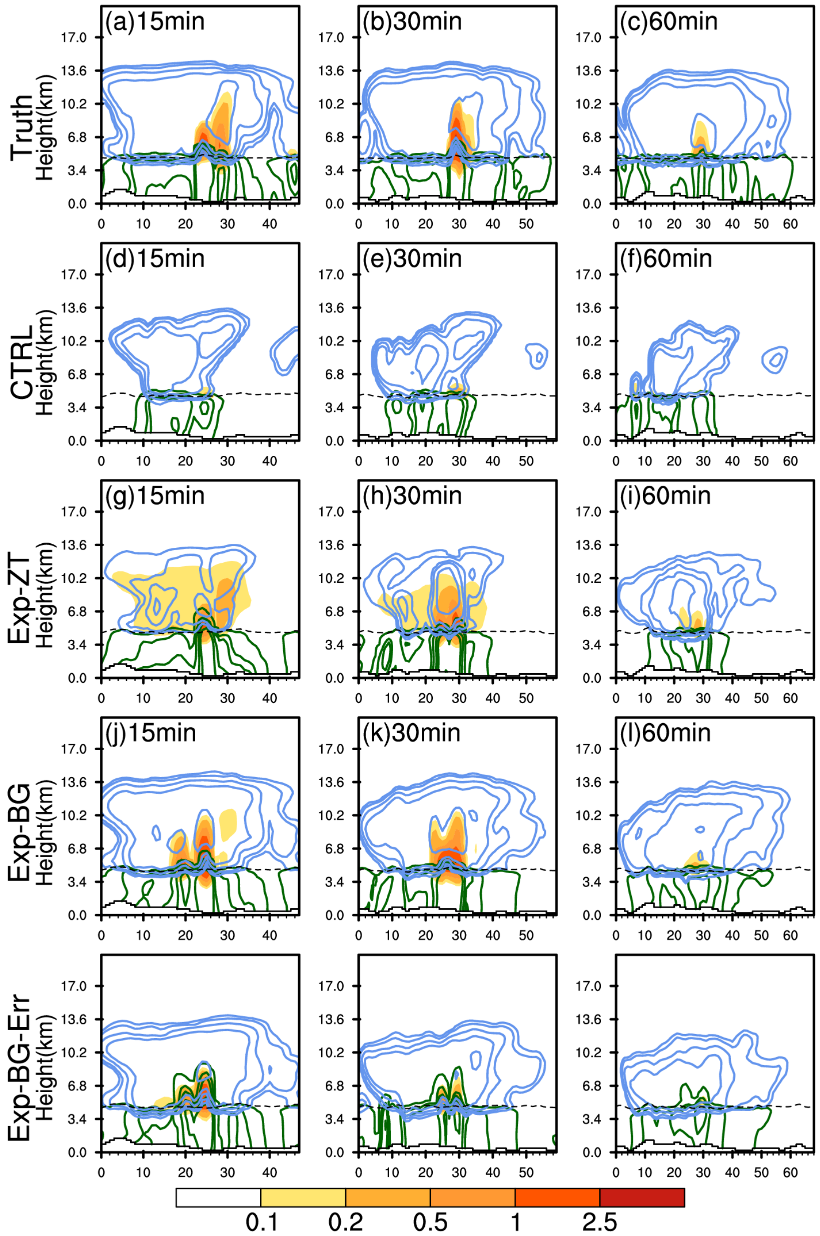

Fig. 8. Vertical cross-sections of the hydrometeor mixing ratio fields: q_g (color shading), q_s (blue contours), q_r (green contours) from (a-c) Truth; (d-f) CTRL; (g-i) Exp-ZT; (j-l) Exp-BG and (m-o) Exp-BG-Err. Legend for the color shadings for q_g (g kg^{-1}) is shown on the bottom. The contour intervals of q_s (g kg^{-1}) are 0.1, 0.2, 0.5, 1.0, 2.5. The contour intervals of q_r (g kg^{-1}) are 0.01, 0.1, 0.2, 0.5, 1.0. The three columns represent the 15, 30 and 60 min forecasts initialized at 1500 UTC, respectively. The locations of the vertical cross sections are shown in line AB in Fig. 3.

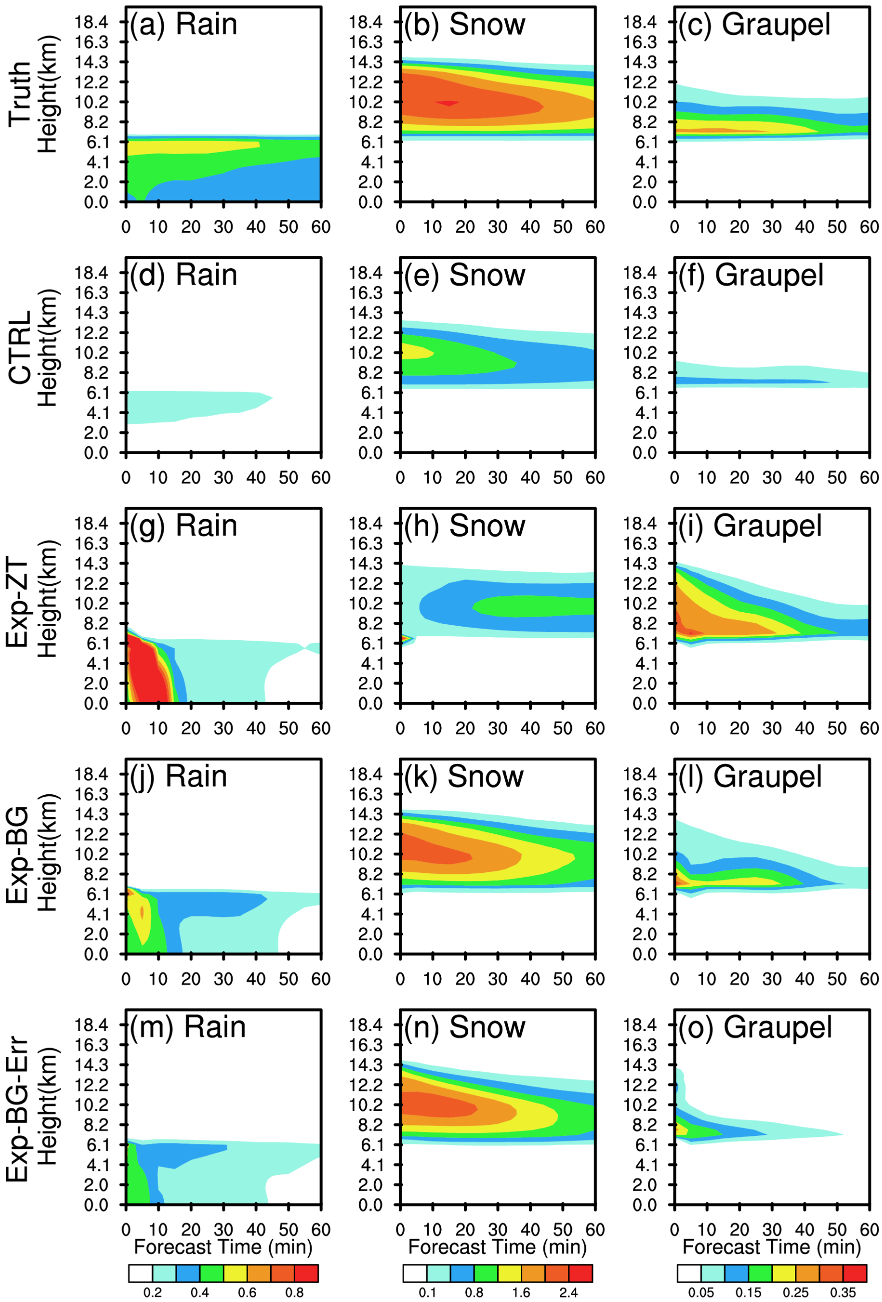

Fig. 9. Vertical cross sections of the temporal evolution of horizontally-averaged hydrometeor mixing ratios in the first 60 minutes over the convective center (units: g kg^{-1}) of (a-c) Truth Run; (d-f) CTRL; (g-i) Exp-ZT; (j-l) Exp-BG; and (m-o) Exp-BG-Err. The forecasts are initiated at 1500 UTC. The calculation region is denoted by the blue box in Fig. 3.

939

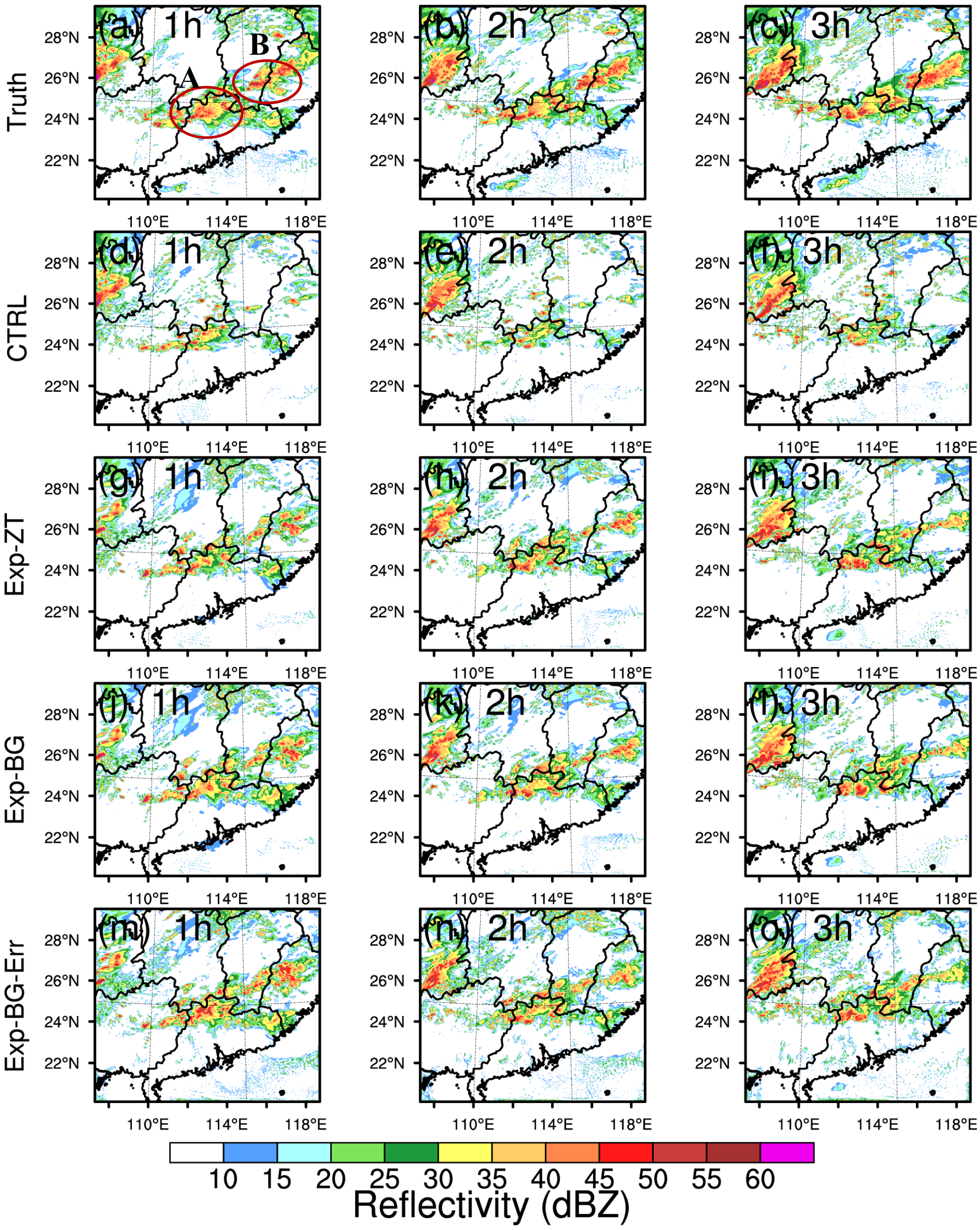

940 Fig. 10. Composite reflectivity forecasts initialized at 1500 UTC from (a-c) Truth; (d-f)
941 CTRL; (g-i) Exp-ZT, (j-l) Exp-BG and (m-o) Exp-BG-Err. The three columns represent the 1-
942 hour forecast, 2-hour forecast and 3-hour forecasts, respectively.

943

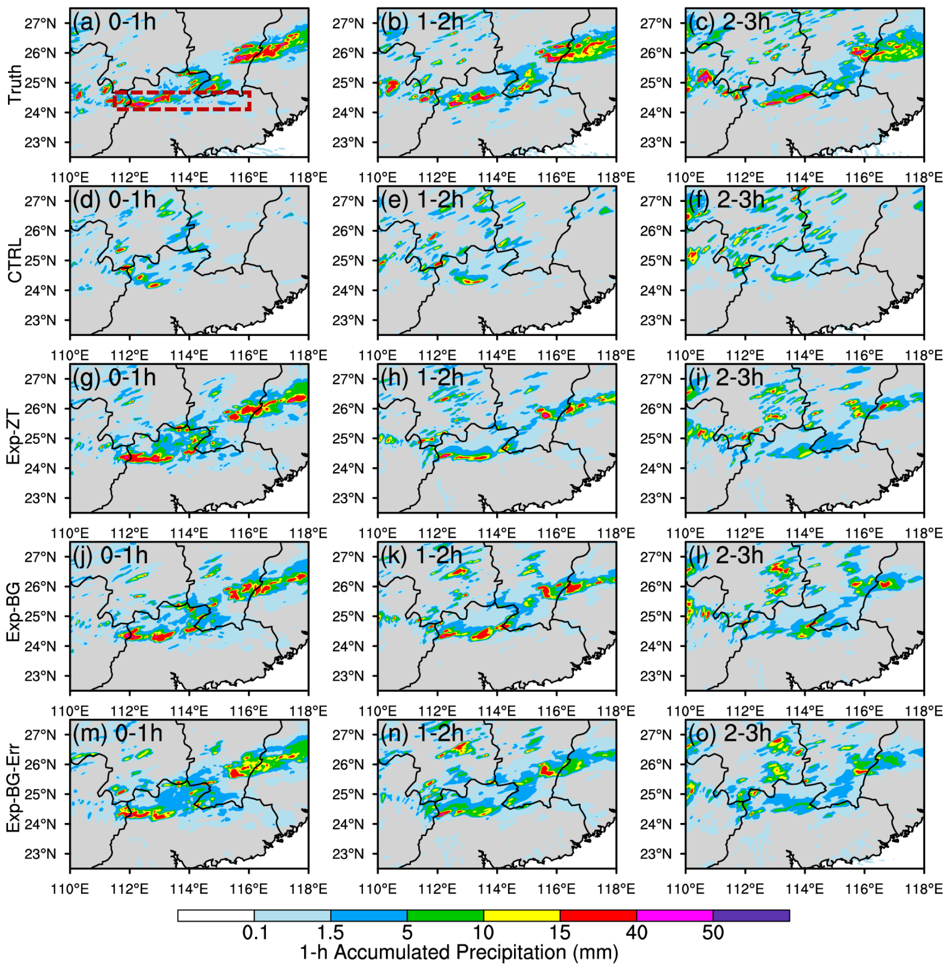

Fig. 11. Hourly accumulated precipitation rates (mm) of the last cycle for (a-c) Truth, (d-f) CTRL, (g-i) Exp-ZT, and (j-l) Exp-BG, and (m-o) Exp-BG-Err. The three columns represent the accumulated precipitation during the first hour, second hour and third hour’s forecast, respectively. The red frame indicates the diagnosed region in Fig. 15 and 16.

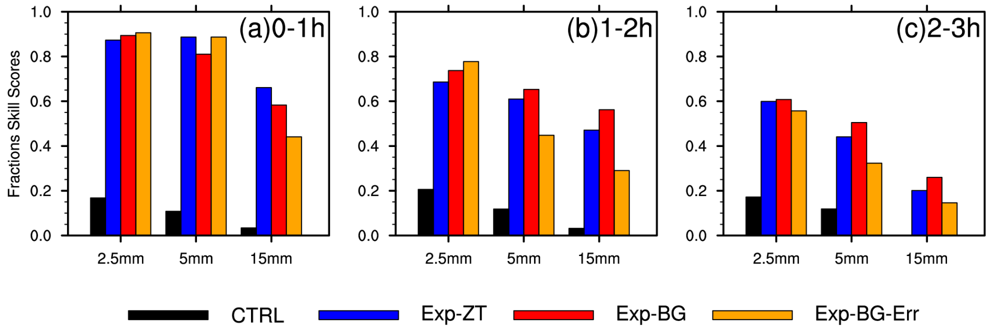

Fig. 12. Averaged Fractions Skill Scores of the hourly-accumulated precipitation forecasts for thresholds of 2.5 mm, 5 mm and 10 mm for CTRL, Exp-ZT, Exp-BG and Exp-BG-Err over the whole cycle. The radius of influence of the neighborhood method used in this study is about 15 km and the scoring area covers the entire precipitation area in Fig. 11.

974

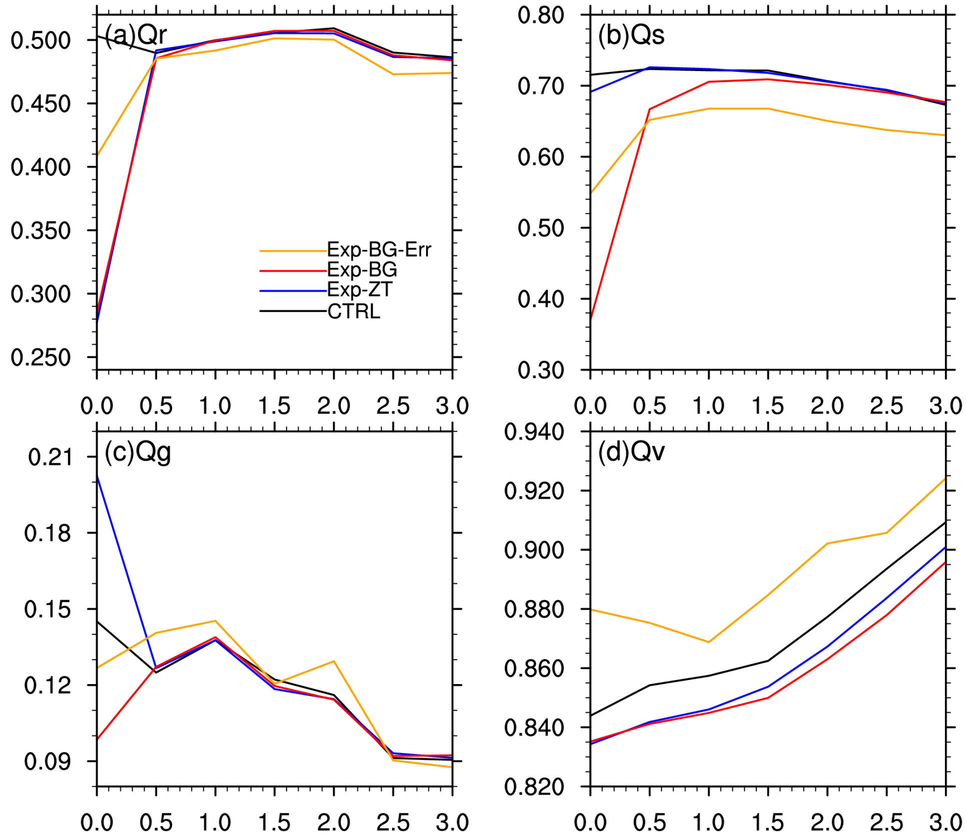

975 Fig. 13. Time series of the analysis and forecast RMSEs of (a) q_r at 850hPa, (b) q_s at 400hPa,
976 (c) q_g at 300hPa and (d) q_v at 700hPa for the whole cycle.

977

978

979

980

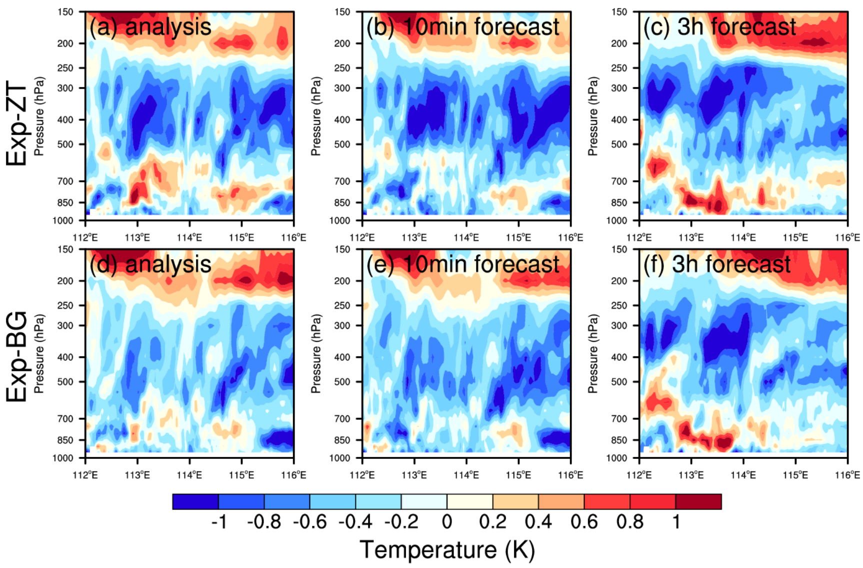

Fig. 14. Cross sections of temperature fields (shaded; K) for (a-c) the difference between Exp-ZT and the Truth Run and (d-f) the difference between Exp-ZT and the Truth Run over the rainfall center from 24.2°N to 24.8°N. The rainfall center is denoted by the red frame in Fig. 11(f). (a, d) are the analyses valid at 1700 UTC. (b, e) are the 10-min forecasts initiated at 1700UTC. (c, f, i) are the 3-hour forecasts initiated at 1700 UTC.

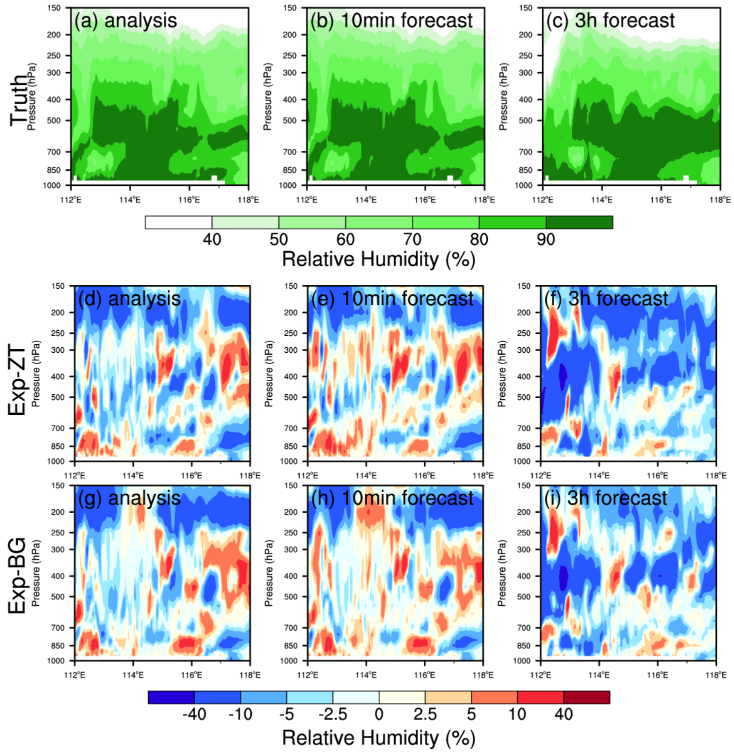

Fig 15. Cross sections of relative humidity fields (shaded; %) for (a-c) Truth, (d-f) the difference between Exp-ZT and the Truth Run, and (g-i) the difference between Exp-BG and the Truth Run over the rainfall center from 24.2°N to 24.8°N. The rainfall center is denoted by the red frame in Fig. 11(f). (a, d, g) are the analyses valid at 1700 UTC. (b, e, h) are the 10-min forecasts initiated at 1700 UTC. (c, f, i) are the 3-hour forecasts initiated at 1700 UTC.